

Surface-induced ferromagnetism and anomalous Hall transport at $\text{Zr}_2\text{S}(001)$

Shuyuan Liu¹, Yanwei Luo^{1,2}, Chongze Wang¹, Hyunsoo Jeon¹, Yu Jia³, and Jun-Hyung Cho^{1*}

¹*Department of Physics and Research Institute for Natural Science,*

Hanyang University, 222 Wangsimni-ro, Seongdong-Ku, Seoul 04763, Republic of Korea

²*College of Science, Henan University of Technology, Zhengzhou 450001, People's Republic of China*

³*Key Laboratory for Special Functional Materials of the Ministry of Education,*

Henan University, Kaifeng 475004, People's Republic of China

(Dated: December 13, 2022)

Two-dimensional layered electrides possessing anionic excess electrons in the interstitial spaces between cationic layers have attracted much attention due to their promising opportunities in both fundamental research and technological applications. Using first-principles calculations, we predict that the layered bulk electride Zr_2S is nonmagnetic with massive Dirac nodal-line states arising from $\text{Zr-}4d$ cationic and interlayer anionic electrons. However, the $\text{Zr}_2\text{S}(001)$ surface increases the density of states at the Fermi level due to the surface potential, thereby inducing a ferromagnetic order at the outermost Zr layer via the Stoner instability. Consequently, the time-reversal symmetry breaking at the surface not only generates spin-polarized topological surface states with intricate helical spin textures but also hosts an intrinsic anomalous Hall effect originating from the Berry curvature generated by spin-orbit coupling. Our findings offer a playground to investigate the emergence of ferromagnetism and anomalous Hall transport at the surface of nonmagnetic topological electrides.

I. INTRODUCTION

Surface ferromagnetism has been a longstanding issue in condensed matter physics because of its importance from both the fundamental and technological points of view [1–3]. The surface electronic structure often differs from the bulk one because surface atoms have the reduced coordination number due to their broken bonds. For example, the (001) surface of a $4d$ transition metal Rh increases the density of states (DOS) at the Fermi level E_F via narrowing its associated energy bands, thereby being vulnerable to a surface ferromagnetic instability [4, 5]. Such surface-induced ferromagnetism in otherwise nonmagnetic bulk material can be explained by the Stoner model of itinerant magnetism: i.e., the Stoner criterion [6], where the product of the exchange integral and the surface DOS at E_F in the nonmagnetic state is greater than 1, is satisfied to induce ferromagnetism.

In the past decade, there have been intense research efforts to explore the connections between symmetries and topologies of condensed matter [7, 8]. As a compelling example of symmetry-protected topological states, massless Dirac fermions with fourfold degenerate band crossings of two doubly degenerate bands are jointly protected by the time-reversal symmetry (TRS) T and space inversion symmetry P supplemented by additional crystalline symmetry such as glide mirror symmetry or screw rotation symmetry [9–11]. However, when T or P symmetry is broken, Dirac fermions are transformed into Weyl fermions with twofold degenerate band crossings of two singly degenerate bands [11, 12]. Such symmetry-protected topological states having linear band crossings at nodes or along one-dimensional lines or loops in momentum space can be classified into Dirac, Weyl, Dirac-nodal-line (DNL), or Weyl-nodal-line semimetal states [13–15]. These gapless topological states with the nontrivial topology of bulk bands host spin-polarized surface states with helical spin textures. However, without sufficient symmetry pro-

tection, the degeneracies at such band crossings are lifted to form hybridization gaps via the inclusion of spin-orbit coupling (SOC), which generate the Berry curvature around gapped crossings [16, 17]. Here, we introduce a nonmagnetic bulk system that has massive DNL states with SOC-induced gap openings, but its surface exhibits a ferromagnetic order. The resulting TRS-breaking ferromagnetic surface hosts the emergence of an intrinsic anomalous Hall effect originating from the Berry curvature. By utilizing the spin degree of freedom generated only at surface, it is highly promising to realize anomalous transport phenomena in future spintronics technologies.

Recently, two-dimensional (2D) layered electrides A_2B have aroused great interest for their exotic electronic properties such as low work function, high electron mobility, and spin polarization [16–20]. In such A_2B electrides consisting of a three-atom-thick building block of A - B - A stacks [see Figs. 1(a) and 1(b)], anionic excess electrons reside in the interstitial spaces between positively charged A - B - A cationic layers. The global structure search method has been used to predict various types of 2D layered electrides such as alkaline-earth nitrides [21], rare-earth carbides [21–23], rare-earth pnictides [24], rare-earth chalcogenides [24], rare-earth halides [23, 24], and transition-metal monochalcogenides [25]. To date, the experimentally synthesized 2D electrides are relatively few with (i) nonmagnetic Ca_2N [18], Hf_2S [26], Zr_2S [25], Sr_3CrN_3 [27], Sr_8P_5 [28], and Sr_5P_3 [28], (ii) paramagnetic Y_2C [29–31], and (iii) ferromagnetic Gd_2C [32] and YCl [33]. Interestingly, recent DFT calculations [34, 35] for the nonmagnetic Hf_2S electride predicted the existence of a ferromagnetic order at the $\text{Hf}_2\text{S}(001)$ surface, where the local DOS arising from the surface Hf atoms increases at E_F and thus induces a Stoner instability.

In this paper, we investigate the surface-induced ferromagnetism and its associated anomalous Hall effect in a nonmagnetic bulk electride Zr_2S using first-principles density-functional theory (DFT) calculations. We find that bulk Zr_2S

has a topological band structure with massive DNLs consisting of hybridized Zr-4d cationic and interlayer anionic states, which exhibit a high DOS distribution between -0.3 and -1.3 eV below E_F . However, such hybridized states associated with the topmost Zr layer at the $\text{Zr}_2\text{S}(001)$ surface shift toward E_F due to the surface potential. The resulting increase in the DOS at E_F induces surface ferromagnetism via a Stoner instability. Furthermore, we demonstrate that the (001) surface of the nonmagnetic bulk electrified Zr_2S not only possesses highly spin-polarized topological surface states with intricate helical spin textures but also exhibits a surface anomalous Hall effect originating from the Berry curvature. The present results offer a playground to investigate the intriguing interplay between electrified materials, surface ferromagnetism, and anomalous transport phenomena.

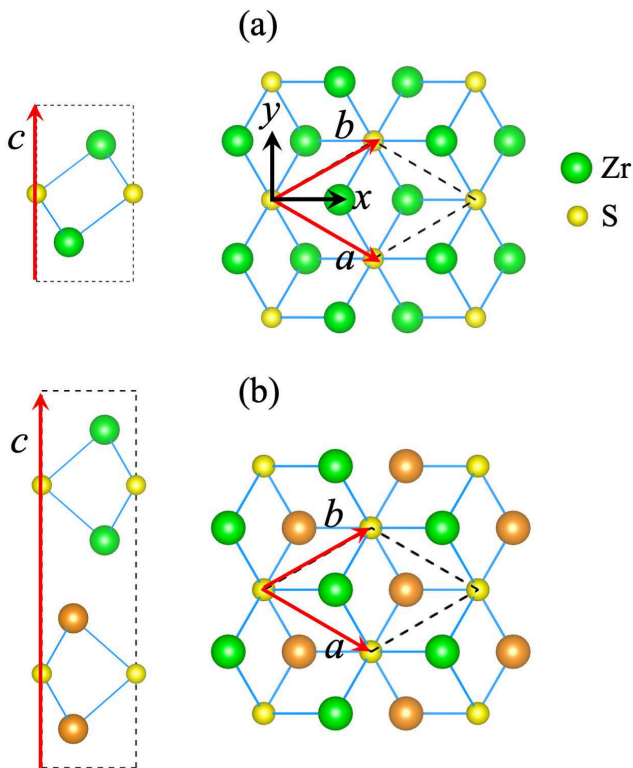


FIG. 1. Side (left panels) and top (right panels) views of the optimized structures of the (a) 1T and (b) 2H phases of bulk Zr_2S . The green and orange balls in panel (b) represent Zr atoms locating in neighboring layers. The lattice parameters a , b , and c are drawn in each unit cell (indicated by the dashed lines). Here, the 1T phase has $a = b = 3.548$ Å and $c = 5.600$ Å, while the 2H phase has $a = b = 3.443$ Å and $c = 11.935$ Å.

II. CALCULATIONAL METHODS

Our first-principles DFT calculations were performed using the Vienna *ab initio* simulation package (VASP) with the projector-augmented wave method [36–38]. The exchange-correlation energy was treated with the generalized-gradient

approximation functional of Perdew-Burke-Ernzerhof [39]. The plane wave basis was employed with a kinetic energy cutoff of 550 eV, and the k -space integration was done with $18 \times 18 \times 12$, $18 \times 18 \times 6$, and $18 \times 18 \times 1$ meshes for the 1T bulk, 2H bulk, and (001) surface, respectively. All atoms were allowed to relax along the calculated forces until all the residual force components were less than 0.005 eV/Å. The phonon spectrum calculation of the 1T bulk was carried out by using the QUANTUM ESPRESSO package [40], with the $6 \times 6 \times 4$ q points. The *ab initio* molecular dynamics simulations were performed by using a $3 \times 3 \times 2$ supercell. The $\text{Zr}_2\text{S}(001)$ surface was simulated using a periodic slab of twelve Zr-S-Zr stacks with ~ 25 Å vacuum in-between adjacent slabs.

III. RESULTS AND DISCUSSION

We begin by optimizing the 1T and 2H phases of bulk Zr_2S using DFT calculations. Here, the 1T phase crystallizes in an octahedral geometry with the space group $P\bar{3}m1$ (No. 164), while the 2H phase crystallizes in a trigonal prismatic geometry with the space group $P6_3/mmc$ (No. 194). Figures 1(a) and 1(b) show the optimized structures of the 1T and 2H phases, respectively. Our spin-polarized calculations for the two phases show that any initial ferromagnetic or antiferromagnetic configuration converges to a nonmagnetic one, indicating that bulk Zr_2S is nonmagnetic. We find that the 1T phase is more energetically favored over the 2H phase by 55.5 meV per 1T unit cell. Interestingly, the preferred 1T phase in Zr_2S contrasts with bulk Hf_2S where the 2H phase has been experimentally synthesized [26]. Hereafter, we focus on the bulk and surface properties of the 1T phase of Zr_2S .

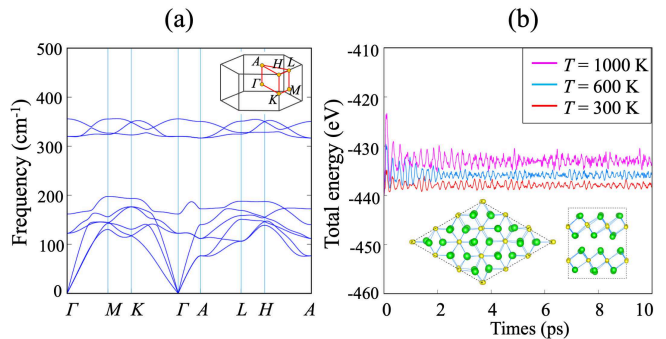


FIG. 2. (a) Calculated phonon spectrum of bulk Zr_2S . The total energy versus time for bulk Zr_2S , computed from *ab initio* molecular dynamics simulations at different temperatures, is displayed in panel (b). The inset in panel (b) shows the top and side views of the simulated structure at 1000 K after 10 ps.

To examine the dynamic stability of bulk Zr_2S , we calculate its phonon spectrum using the density-functional perturbation theory [41, 42]. As shown in Fig. 2(a), there are no imaginary phonon frequencies over the whole Brillouin zone, indicating that bulk Zr_2S is dynamically stable. We further perform *ab initio* molecular dynamics simulations to ensure

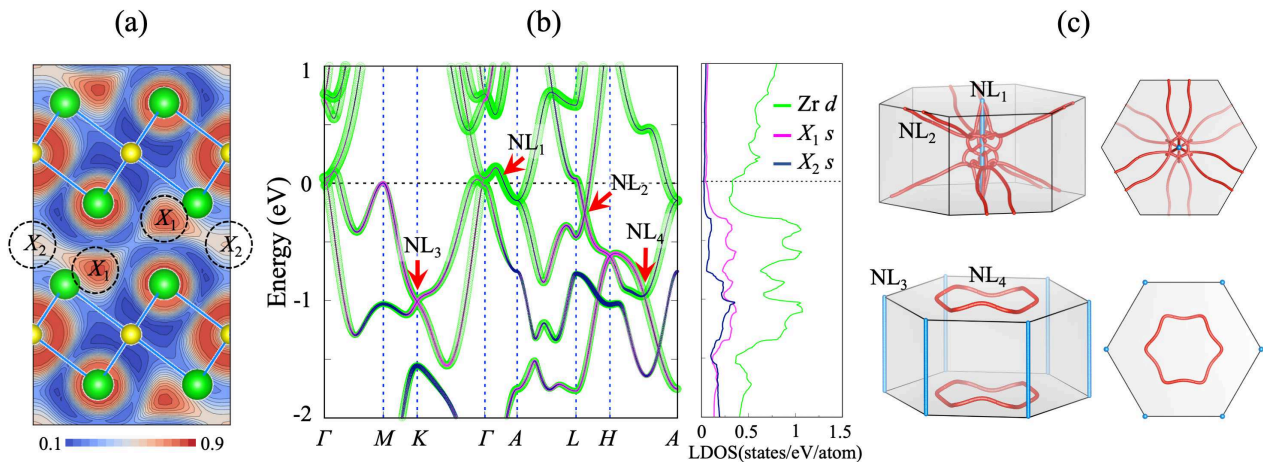


FIG. 3. (a) Calculated ELF of bulk Zr_2S on the $(1\bar{1}0)$ plane with a contour spacing of 0.05. Here, the dashed circles represent X_1 and X_2 anions, the muffin-tin radii of which are chosen as 1 Å. The calculated band structure and partial DOS of bulk Zr_2S are displayed in panel (b), where the projected bands on Zr- $4d$ and X_1 -, X_2 - s -like orbitals are represented by circles whose radii are proportional to the weights of the corresponding orbitals. In panel (b), the red arrows indicate various nodal lines NL_1 , NL_2 , NL_3 , and NL_4 (see text) around E_F whose dispersions over the Brillouin zone are drawn in panel (c). The right panels in (c) show the top views of nodal lines.

the thermodynamic stability of bulk Zr_2S . Figure 2(b) shows the time evolution of total energies at different temperatures of 300, 600, and 1000 K. We find that the total energy at each temperature is well converged without large deviations. Specifically, the top and side views of the simulated structure at 1000 K after 10 ps show that the layered structure is preserved without any bond breakage. It is thus likely that bulk Zr_2S would be thermodynamically stable even at a high temperature of ~ 1000 K. Recently, Zr_2S was experimentally synthesized with a polymorphic phase with the $P\bar{3}m1$ (equivalent to the 1T phase) and $Pnmm$ structures [25]. Further experimental synthetic works will be demanded for the formation of a single 1T phase in the future.

Figure 3(a) shows the electron localization function (ELF) of bulk Zr_2S . It is seen that anionic excess electrons are well localized at the positions marked as X_1 and X_2 in the inter-layer space, demonstrating that bulk Zr_2S is characterized as a 2D layered electride. In Fig. 3(b), the calculated band structure of bulk Zr_2S shows that Zr- $4d$ cationic and interstitial anionic states are strongly hybridized in the energy range between ≈ -0.3 and ≈ -1.3 eV below E_F , giving rise to several common peaks in their partial densities of states. We note that S- $3s$ and S- $3p$ orbitals are located below -3 eV (see Fig. S1 in the Supplemental Material [43]), indicating that S atoms hardly participate in hybridization with interstitial anionic states. Interestingly, at the $Zr_2S(001)$ surface, the hybridized Zr- $4d$ cationic and interstitial anionic states associated with the topmost Zr layer are shifted toward E_F , thereby inducing a surface ferromagnetic instability, as discussed below.

Using the tight-binding (TB) Hamiltonian with a basis of maximally localized Wannier functions [45, 46], we investigate the topological properties of bulk Zr_2S . The TB Wannier bands of bulk Zr_2S agree well with the corresponding DFT

ones calculated using the VASP code (see Fig. S2 in the Supplemental Material [43]). As shown in Figs. 3(b) and 3(c), we find fourfold degenerate band touching points around E_F , forming nodal lines NL_1 and NL_3 along the $\Gamma-A$ and $K-H$ paths, respectively, and nodal loops NL_2 and NL_4 . It is noted that the NL_2 and NL_4 DNLs are respected by the P symmetry, whereas the NL_1 (NL_3) DNL is respected by the C_{3z} (C_{3z} and P) symmetry [47] (see Fig. S3 in the Supplemental Material [43]). The nontrivial topological characterization of DNLs is identified by calculating the topological Z_2 index [48], defined as $\zeta_1 = \frac{1}{\pi} \oint_c dk \cdot A(k)$, along a closed loop encircling each DNL. Here, $A(k) = -i \langle u_k | \partial_k | u_k \rangle$ is the Berry connection for the related Bloch states. We obtain $\zeta_1 = \pm 1$ for the DNLs, indicating that they are stable against perturbations without breaking involved symmetries. However, by taking into account SOC, the fourfold degeneracy of DNLs is lifted to open gaps, thereby leading to massive DNLs around E_F .

Next, we investigate the electronic structure of the $Zr_2S(001)$ surface. Figure 4(a) shows the band structure of the nonmagnetic $Zr_2S(001)$ surface in the absence of SOC. We find that there are two surface states SS_1 and SS_2 along the $\Gamma-K-M$ path near E_F , which are composed of the hybridized Zr- $14d$ cationic and interstitial $X_1(X_2)$ - s -like anionic states. Here, Zr-1, X_1 , and X_2 represent Zr atom and interstitial anions at the topmost surface layer [see Fig. 4(b)]. It is noted that the number of electrons within the muffin-tin sphere of the surface X_1 (X_2) anion is 0.321 (0.204) electrons [see Fig. 4(b)], different from the corresponding bulk value of 0.570 (0.394) electrons [see Fig. 3(a)]. Figure 4(c) shows the local DOS (LDOS) projected on the Zr-1 and Zr-2 atoms [see Fig. 4(b)]. We find that the LDOS of Zr-1 at E_F increases significantly compared to those of Zr-2 and bulk Zr [see Fig. 3(b)]. This dramatic change of Zr- $4d$ states together with the rearrangement of interstitial anionic electrons at $Zr_2S(001)$ manifests strong sur-

face effects. Due to the high LDOS of Zr-1 at E_F , the Stoner criterion may be satisfied to drive a ferromagnetic instability at the $\text{Zr}_2\text{S}(001)$ surface. Indeed, the ferromagnetic phase is found to be energetically favored over the nonmagnetic one by 5.6 meV per Zr surface atom. For the ferromagnetic phase, the LDOS of Zr-1 shows that the spin-up and -down states are separated by ≈ 0.261 eV (see Fig. S4 in the Supplemental Material [43]). By dividing this exchange splitting by the magnetic moment of Zr-1, we can estimate the Stoner parameter I , which in turn satisfies the Stoner criterion $I \cdot D(E_F) > 1$ (see Fig. S4 [43]). Here, $D(E_F)$ is the LDOS of Zr-1 at E_F , obtained from the nonmagnetic surface. Thus, we can say that surface ferromagnetism emerging at the $\text{Zr}_2\text{S}(001)$ surfaces is driven by the Stoner instability due to an increase in the surface DOS at E_F . To estimate the Curie temperature T_c , we perform spin-polarized DFT calculations for various antiferromagnetic surface configurations (see Fig. S5 [43]). We find that the lowest antiferromagnetic configuration is less stable than the ferromagnetic one by 11.1 meV per Zr surface atom. Using the mean field approximation [44], we estimate a T_c of ≈ 85 K at the $\text{Zr}_2\text{S}(001)$ surface.

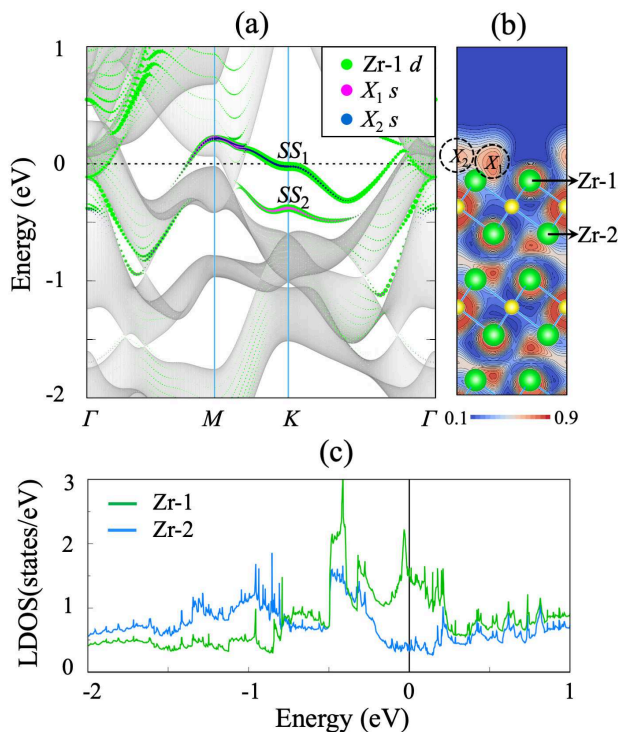


FIG. 4. (a) Calculated band structure of the nonmagnetic phase of the $\text{Zr}_2\text{S}(001)$ surface. Here, the surface states SS_1 and SS_2 are projected onto the Zr-1 d , X_1 s -, and X_2 s -like orbitals where the radii of circles are proportional to the weights of the corresponding orbitals. The grey shaded region indicates the projection of bulk states. The ELF of the $\text{Zr}_2\text{S}(001)$ surface with a contour spacing of 0.05 is displayed in panel (b), where the dashed circles represent X_1 and X_2 anions locating at the topmost surface layer. The calculated LDOS of Zr-1 and Zr-2 atoms at the $\text{Zr}_2\text{S}(001)$ surface are given in panel (c).

Figures 5(a) and 5(b) show the band structure and spin den-

sity of the ferromagnetic $\text{Zr}_2\text{S}(001)$ surface, respectively, calculated without including SOC. We find that the SS_1 and SS_2 surface states are spin-polarized to exhibit surface ferromagnetism. Consequently, the spin density is mostly distributed around the Zr-1 layer, while it is significantly reduced at the Zr-2 layer [see Fig. 5(b)]. The calculated spin magnetic moments integrated within the muffin-tin spheres around Zr-1, X_1 , and X_2 at the topmost surface layer are $0.189 \mu_B$, $0.056 \mu_B$, and $0.053 \mu_B$, respectively (see Table I). It is noted that the magnitude of the spin magnetic moment of Zr-2 decreases to $-0.014 \mu_B$ and the Zr-1 and Zr-2 spins are antiferromagnetically coupled to each other. By including SOC, we calculate the magnetic anisotropy energy (MAE) at the $\text{Zr}_2\text{S}(001)$ surface. Figure 5(c) displays the angular dependence of MAE on the xy -, yz -, and zx -planes. We find that the easy axis is out-of-plane with a MAE of 0.024 meV per Zr surface atom. As shown in Fig. 5(c), the MAE on the xy -plane is isotropic, whereas that on the yz - or zx -plane strongly depends on the angle ϕ relative to the z direction. To explore the topological nature of surface states associated with the gapped bulk DNLs, we calculate their spin texture at E_F with including SOC. Figure 5(d) shows the calculated Fermi surface at the ferromagnetic $\text{Zr}_2\text{S}(001)$ surface. We find that the minority-spin SS_1 surface state forming a hole pocket around the M point and an electron pocket along the $\Gamma - K$ path exhibits a helical spin texture with spin-momentum locking, indicating nontrivial topological surface states without backscattering [49, 50].

TABLE I. Calculated spin magnetic moments (in unit of μ_B per Zr atom) of Zr-1 and Zr-2 at the $\text{Zr}_2\text{S}(001)$ surface. The values of X_1 and X_2 at the topmost surface layer are also given.

	Zr-1	Zr-2	X_1	X_2
Magnetic moment	0.189	-0.014	0.056	0.053

Finally, we examine the existence of an anomalous transport behavior at the ferromagnetic $\text{Zr}_2\text{S}(001)$ surface. Using the Kubo-formula approach in the linear response scheme [51], we calculate the intrinsic anomalous Hall conductivity σ_{xy} originating from the Berry curvature. Figure 6(a) shows σ_{xy} versus energy plot, obtained by integrating the z component of Berry curvature (Ω_z) of all the occupied bulk and surface states over the surface Brillouin zone. We find that σ_{xy} has a negative value of $\approx -0.5 e^2/h$ at E_F , while it exhibits a large positive peak of $\approx 1.5 e^2/h$ at -0.084 eV below E_F . Thus, as hole doping shifts E_F to -0.084 eV (see Fig. S6 in the Supplemental Material [43]), σ_{xy} can increase significantly. Figures 6(b) and 6(c) display Ω_z distributions integrated in the two different energy ranges: one is the R_I region between -0.148 and -0.015 eV and the other is the R_{II} region between -0.015 eV and E_F . For the R_I region, there are the “hotspots” of positive Ω_z arising from the electron pocket of the surface state along the $\Gamma - K$ path and the gapped NL_1 DNL around the Γ point. Meanwhile, for the R_{II} region, the latter gapped DNL mostly contributes to more

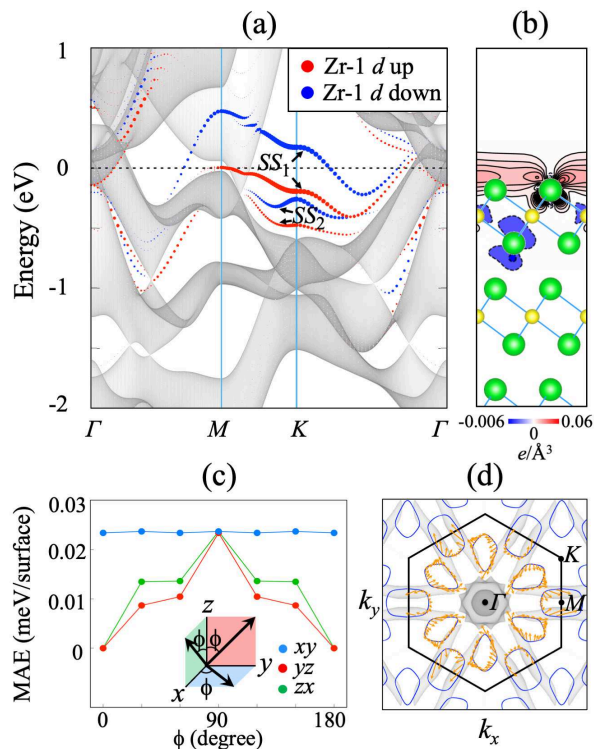


FIG. 5. (a) Calculated band structure of the ferromagnetic phase of the $\text{Zr}_2\text{S}(001)$ surface. Here, the spin-polarized surface states SS_1 and SS_2 are projected onto the Zr-1 d orbitals where the radii of circles are proportional to the weights of the corresponding orbitals. The grey shaded region indicates the projection of bulk states. In panel (b), the spin density at the $\text{Zr}_2\text{S}(001)$ surface is drawn with a contour spacing of $0.005 \text{ e}/\text{\AA}^3$. The angular dependence of MAE with respect to ϕ on the xy -, yz -, and zx -planes is displayed in panel (c), where the minimum energy is set to zero. The spin texture of surface states on the Fermi surface is drawn in panel (d), where the arrows represent the S_x and S_y components along the horizontal and vertical directions, respectively. In panel (d), the blue lines represent the Fermi surface of the minority-spin SS_1 surface state, while the grey shaded region indicates the Fermi surface projected by bulk states.

positive and negative Ω_z values. Therefore, the gapped NL_1 DNL plays an important role in σ_{xy} around E_F , yielding an anomalous electronic transport behavior.

IV. CONCLUSION

Based on first-principles DFT calculations, we have predicted a ferromagnetic instability at the (001) surface of the 2D layered electride Zr_2S , the bulk of which is nonmagnetic. In contrast to bulk Zr_2S where hybridized Zr-4d cationic and interlayer anionic states are located away below E_F , we found that the $\text{Zr}_2\text{S}(001)$ surface has a high DOS at E_F arising from such hybridized states, thereby inducing surface ferromagnetism via a Stoner instability. As a result, the $\text{Zr}_2\text{S}(001)$ surface not only possesses highly spin-polarized topological

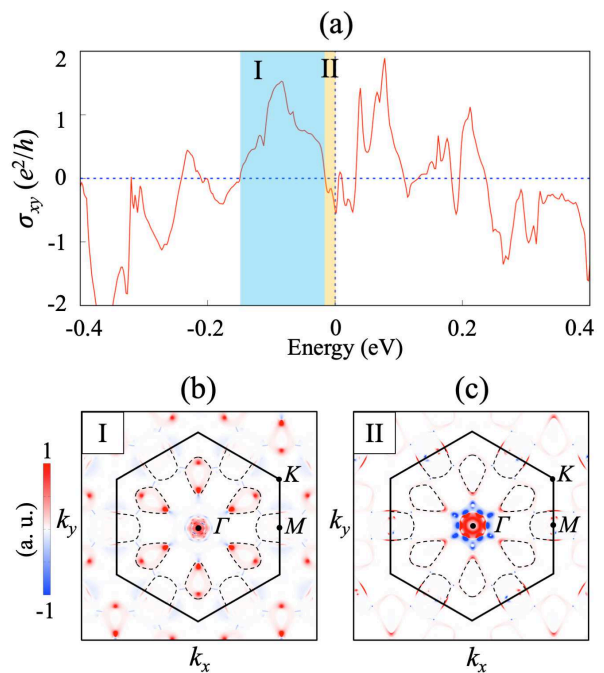


FIG. 6. (a) Energy dependence of σ_{xy} and (b) (c) Ω_z distribution in the two energy regions I and II. In panels (b) and (c), red and blue areas indicate the “hotspots” of positive and negative Ω_z , respectively. The dashed lines in panels (b) and (c) represent the Fermi surface of the minority-spin SS_1 surface state.

surface states associated with massive DNLs but also hosts an intrinsic anomalous Hall effect originating from the Berry curvature generated by SOC. Therefore, our findings provide a novel platform to investigate the intriguing interplay between electride materials, surface ferromagnetism, and anomalous Hall transport which will be promising for future spintronics technologies.

Acknowledgements. This work was supported by the National Research Foundation of Korea (NRF) grant funded by the Korean Government (Grant No. 2022R1A2C1005456), by BrainLink program funded by the Ministry of Science and ICT through the National Research Foundation of Korea (Grant No. 2022H1D3A3A01077468), and by the National Natural Science Foundation of China (Grant No. 12074099). The calculations were performed by the KISTI Supercomputing Center through the Strategic Support Program (Program No. KSC-2022-CRE-0073) for the supercomputing application research.

S. L. and Y. L. contributed equally to this work.

* Corresponding author: chojh@hanyang.ac.kr

[1] C. Kittel, Theory of the structure of ferromagnetic domains in films and small particles, *Phys. Rev.* **70**, 965 (1946).

- [2] U. Gradmann, Ferromagnetism near surfaces and in thin films, *Appl. Phys.* **3**, 161 (1974).
- [3] A. Sundaresan, C.N.R. Rao, Ferromagnetism as a universal feature of inorganic nanoparticles, *Nano. Today* **4**, 96 (2009).
- [4] J.-H. Cho and M.-H. Kang, Possibility of a ferromagnetic Rh (001) surface: A plane-wave-basis partial-core pseudopotential approach, *Phys. Rev. B* **52**, 13805 (1995).
- [5] J.-H. Cho and M. Scheffler, Surface relaxation and ferromagnetism of Rh (001), *Phys. Rev. Lett.* **78**, 1299 (1997).
- [6] Edmund C Stoner F R S, Ferromagnetism, *Rep. Prog. Phys.* **11**, 43 (1947).
- [7] Z. Song, Z. Fang, and C. Fang, (d-2)-Dimensional Edge States of Rotation Symmetry Protected Topological States, *Phys. Rev. Lett.* **119**, 246402 (2017).
- [8] X. Chen, Z.-C. Gu, Z.-X. Liu, and X.-G. Wen, Symmetry-protected topological orders in interacting bosonic systems, *Science* **338**, 1604 (2012).
- [9] N. P. Armitage, E. J. Mele, and A. Vishwanath, Weyl and Dirac semimetals in three-dimensional solids, *Rev. Mod. Phys.* **90**, 015001 (2018).
- [10] B.-J. Yang and N. Nagaosa, Classification of stable three-dimensional Dirac semimetals with nontrivial topology, *Nat. Commun.* **5**, 4898 (2014).
- [11] Z. Lin, C. Wang, P. Wang, S. Yi, L. Li, Q. Zhang, Y. Wang, Z. Wang, H. Huang, Y. Sun, Y. Huang, D. Shen, D. Feng, Z. Sun, J.-H. Cho, C. Zeng, and Z. Zhang, Dirac fermions in antiferromagnetic FeSn kagome lattices with combined space inversion and time-reversal symmetry, *Phys. Rev. B* **102**, 155103 (2020).
- [12] L. Liu, C. Wang, J. Li, X.-Q. Chen, Y. Jia, and J.-H. Cho, Two-dimensional topological semimetal states in monolayer Cu₂Ge, Fe₂Ge, and Fe₂Sn, *Phys. Rev. B* **101**, 165403 (2020).
- [13] R. Yu, Z. Fang, X. Dai, and H. Weng, Topological nodal line semimetals predicted from first-principles calculations, *Front. Phys.* **12**, 127202 (2017).
- [14] S. Y. Yang, H. Yang, E. Derunova, S. S. P. Parkin, B. Yan, and M. N. Ali, Symmetry demanded topological nodal-line materials, *Adv. Phys.: X* **3**, 1414631 (2018).
- [15] R. Li, H. Ma, X. Cheng, S. Wang, D. Li, Z. Zhang, Y. Li, and X.-Q. Chen, Dirac node lines in pure alkali earth metals, *Phys. Rev. Lett.* **117**, 096401 (2016).
- [16] S. Liu, C. Wang, L. Liu, J.-H. Choi, H.-J. Kim, Y. Jia, C. H. Park, and J.-H. Cho, Ferromagnetic Weyl fermions in two-dimensional layered electride Gd₂C, *Phys. Rev. Lett.* **125**, 187203 (2020).
- [17] L. Liu, C. Wang, S. Yi, D. K. Kim, C. H. Park, and J.-H. Cho, Theoretical prediction of Weyl fermions in the paramagnetic electride Y₂C, *Phys. Rev. B* **99**, 220401(R) (2019).
- [18] K. Lee, S. W. Kim, Y. Toda, S. Matsuishi, and H. Hosono, Dicalcium nitride as a two-dimensional electride with an anionic electron layer, *Nature (London)* **494**, 336 (2013).
- [19] S. Liu, W. Li, S. W. Kim, and J.-H. Choi, Decisive Role of Interlayer Ionic Couplings for the Electronic Properties of Two-Dimensional Layered Electrides, *J. Phys. Chem. C* **124**, 1398 (2020).
- [20] S. Liu, C. Wang, H. Jeon, J. Kim, and J.-H. Cho, Interlayer exchange interaction driven topological phase transition in antiferromagnetic electride Gd₂O, *Phys. Rev. B* **105**, L041406 (2022).
- [21] T. Tada, S. Takemoto, S. Matsuishi, and H. Hosono, High-throughput ab initio screening for two-dimensional electride materials, *Inorg. Chem.* **53**, 10347 (2014).
- [22] T. Inoshita, S. Jeong, N. Hamada, and H. Hosono, Exploration for two-dimensional electrides via database screening and *ab Initio* calculation, *Phys. Rev. X* **4**, 031023 (2014).
- [23] J. Zhou, L. Shen, M. Yang, H. Cheng, W. Kong, and Y. P. Feng, Discovery of hidden classes of layered electrides by extensive high-throughput material screening, *Chem. Mater.* **31**, 1860 (2019).
- [24] Y. Zhang, H. Wang, Y. Wang, L. Zhang, and Y. Ma, Computer-assisted inverse design of inorganic electrides, *Phys. Rev. X* **7**, 011017 (2017).
- [25] S. H. Kang, D. Thapa, B. Regmi, S. Ren, Y.-M. Kim, S.-G. Kim, and S. W. Kim, Chemically stable low-dimensional electrides in transition metal-rich monochalcogenides: theoretical and experimental explorations, *J. Am. Chem. Soc.* **144**, 4496 (2022).
- [26] S. H. Kang, J. Bang, K. Chung, C. N. Nandadasa, G. Han, S. Lee, K. H. Lee, K. Lee, Y. Ma, S. H. Oh, S.-G. Kim, Y.-M. Kim, and S. W. Kim, Water- and acid-stable self-passivated dihafnium sulfide electride and its persistent electrocatalytic reaction, *Sci. Adv.* **6**, eaba7416 (2020).
- [27] P. Chanhom, K. E. Fritz, L. A. Burton, J. Kloppenburg, Y. Filinchuk, A. Senyshyn, M. Wang, Z. Feng, N. Insin, J. Suntivich *et al.*, Sr₃CrN₃: A new electride with a partially filled d-Shell transition metal, *J. Am. Chem. Soc.* **141**, 10595 (2019).
- [28] J. Wang, K. Hanzawa, H. Hiramatsu, J. Kim, N. Umezawa, K. Iwanaka, T. Tada, and H. Hosono, Exploration of stable strontium phosphide-based electrides: theoretical structure prediction and experimental validation, *J. Am. Chem. Soc.* **139**, 15668 (2017).
- [29] X. Zhang, Z. Xiao, H. Lei, Y. Toda, S. Matsuishi, T. Kamiya, S. Ueda, and H. Hosono, Two-Dimensional transition-Metal electride Y₂C, *Chem. Mater.* **26**, 6638 (2014).
- [30] J. Park, K. Lee, S. Y. Lee, C. N. Nandadasa, S. Kim, K. H. Lee, Y. H. Lee, H. Hosono, S.-G. Kim, and S. W. Kim, Strong localization of anionic electrons at interlayer for electrical and magnetic anisotropy in two-dimensional Y₂C electride, *J. Am. Chem. Soc.* **139**, 615 (2017).
- [31] M. Hiraishi, K. M. Kojima, I. Yamauchi, H. Okabe, S. Takeshita, A. Koda, R. Kadono, X. Zhang, S. Matsuishi, H. Hosono, K. Hirata, S. Otani, and N. Ohashi, Electronic correlation in the quasi-two-dimensional electride Y₂C, *Phys. Rev. B* **98**, 041104(R) (2018).
- [32] S. Y. Lee, J.-Y. Hwang, J. Park, C. N. Nandadasa, Y. Kim, J. Bang, K. Lee, K. H. Lee, Y. Zhang, Y. Ma, H. Hosono, Y. H. Lee, S.-G. Kim, and S. W. Kim, Ferromagnetic quasi-atomic electrons in two-dimensional electride, *Nat. Commun.* **11**, 1526 (2020).
- [33] H. Y. Song, B. I. Yoo, J.-H. Choi, S.-H. Kang, J. Bang, W. Li, C. N. Nandadasa, D. Thapa, D. Yoon, M. J. Han, K. H. Lee, S. G. Kim, K. Lee, and S. W. Kim, Van der Waals electride: toward intrinsic two-dimensional ferromagnetism of spin-polarized anionic electrons, *Mater. Today Phys.* **20**, 100473 (2021).
- [34] S. Liu, C. Wang, H. Jeon, Y. Jia, and J.-H. Cho, Emerging two-dimensional magnetism in nonmagnetic electrides Hf₂X (X=S, Se, Te), *Phys. Rev. B* **105**, L220401 (2022).
- [35] J. Zhang, D. Xu, X. Qiu, N. Zhao, Z. Lu and K. Liu, Magnetic surface on nonmagnetic bulk of electride Hf₂S, arXiv preprint arXiv: **2207**, 07042 (2022).
- [36] G. Kresse and J. Hafner, Ab initio molecular dynamics for open-shell transition metals, *Phys. Rev. B* **48**, 13115 (1993).
- [37] G. Kresse and J. Furthmüller, Efficiency of ab-initio total energy calculations for metals and semiconductors using a plane-wave basis set, *Comput. Mater. Sci.* **6**, 15 (1996).
- [38] P. E. Blöchl, Projector augmented-wave method, *Phys. Rev. B* **50**, 17953 (1994).
- [39] J. P. Perdew, K. Burke, and M. Ernzerhof, Generalized gradient approximation made simple, *Phys. Rev. Lett.* **77**, 3865 (1996);

- 78**, 1396(E) (1997).
- [40] P. Giannozzi, S. Baroni, N. Bonini, M. Calandra, R. Car, C. Cavazzoni, D. Ceresoli, G. L. Chiarotti, M. Cococcioni, I. Dabo *et al.*, QUANTUM ESPRESSO: a modular and open-source software project for quantum simulations of materials, *J. Phys.: Condens. Matter* **21**, 395502 (2009).
- [41] A. Togo and I. Tanaka, First principles phonon calculations in materials science, *Scr. Mater.* **108**, 1 (2015).
- [42] K. Parlinski, Z. Q. Li and Y. Kawazoe, First-Principles determination of the soft mode in cubic ZrO_2 , *Phys. Rev. Lett.* **78**, 4063 (1997).
- [43] See Supplemental Material at <http://link.aps.org/supplemental/xxxx> for the PDOS of bulk Zr_2S , the comparison of the electronic bands obtained using the DFT and tight-binding Hamiltonian calculations, breaking the inversion symmetry in bulk Zr_2S , the Stoner instability and Curie temperature at the $Zr_2S(001)$ surface, and the hole doping at the $Zr_2S(001)$ surface, which includes Refs. [12, 44].
- [44] G. S. Rushbrooke and P. J. Wood, On the Curie points and high temperature susceptibilities of Heisenberg model ferromagnetics, *Mol. Phys.* **1**, 257 (1958); On the high temperature staggered susceptibility of Heisenberg model antiferromagnetics, **6**, 409 (1963).
- [45] A. A. Mostofi, J. R. Yates, Y.-S. Lee, I. Souza, D. Vanderbilt, and N. Marzari, wannier90: A tool for obtaining maximally-localised Wannier functions, *Comput. Phys. Commun.* **178**, 685 (2008).
- [46] Q. S. Wu, S. N. Zhang, H.-F. Song, M. Troyer, and A. A. Soluyanov, WannierTools: An open-source software package for novel topological materials, *Comput. Phys. Commun.* **224**, 405 (2018).
- [47] K. Kim, J. Seo, E. Lee, K.-T. Ko, B. S. Kim, B. G. Jang, J. M. Ok, J. Lee, Y. J. Jo, W. Kang, J. H. Shim, C. Kim, H. W. Yeom, B. Il Min, B.-J. Yang, and J. S. Kim, Large anomalous Hall current induced by topological nodal lines in a ferromagnetic van der Waals semimetal, *Nat. Mater.* **17**, 794 (2018).
- [48] C. Fang, H. Weng, X. Dai, and Z. Fang, Topological nodal line semimetals, *Chin. Phys. B* **25**, 117106 (2016).
- [49] N. P. Armitage, E. J. Mele, and A. Vishwanath, Weyl and Dirac semimetals in three-dimensional solids, *Rev. Mod. Phys.* **90**, 015001 (2018).
- [50] X.-Q. Sun, S.-C. Zhang, and Z. Wang, Helical spin order from topological Dirac and Weyl semimetals, *Phys. Rev. Lett.* **115**, 076802 (2015).
- [51] D. Xiao, M.-C. Chang, and Q. Niu, Berry phase effects on electronic properties, *Rev. Mod. Phys.* **82**, 1959 (2010).